RSC Advances

PAPER

View Article Online
View Journal | View Issue

Cite this: *RSC Adv.*, 2026, **16**, 27809

Topological isomers in lanthanide–chloranilate coordination polymers: synthesis, structure and CO_2 adsorption properties

Kenika Khotchasanthong, [a] Chombongkot Sricharoen, [a] Pacharapon Jearanaiwiwat, [a] Kunlanit Chinchan, [a] Sakchai Laksee, [b] Bunyarat Rungtaweevoranit, [c] Mongkol Sukwattanasinitt [d] and Kittipong Chainok *[ae]

The effect of lanthanide contraction on the self-assembly of two-dimensional (2D) topological isomers in lanthanide coordination polymers (LnCPs) is presented in this work. Hydrothermal reactions involving $LnCl_3$ and chloranilic acid (H_2ca) afforded good yields of ten LnCPs with the general formula $[Ln(ca)_{1.5}(H_2O)_3]\cdot xH_2O$ (**1Ln**; Ln = Pr, Nd; **2Ln**; Ln = Sm, Eu, Gd, Tb, Dy, Er, Tm, Yb; x = 3.5–5). The isostructural compounds crystallize in the centrosymmetric triclinic $P\bar{1}$ space group and display 2D layered networks featuring topologically distinct isomers, specifically honeycomb for **1Ln** and brick-wall for **2Ln**. The lattice water molecules are located in interlayered spaces with the number of water molecules per formula unit increasing as the ionic radii of Ln^{3+} decrease. The incorporation of the semi-rigid rod 4,4′-bipyridine (4,4′-bipy) into brick-wall 2D networks aims to establish a porous 3D pillared framework, leading to the creation of an intercalation network comprising the guest 4,4′-bipy and lattice water molecules, $[Ln(ca)_{1.5}(H_2O)_2]\cdot 2H_2O\cdot$4,4′-bipy (**3Ln**; Ln = Tm, Yb). The physicochemical properties of the isomers **1Ln** and **2Ln** were clearly illustrated, highlighting their unique structural features, thermal stability, and adsorption characteristics. At both low pressure (1 bar) and elevated pressure (up to 20 bar), the thermally activated brick-wall network **2Yb** demonstrated better absorption of CO_2 relative to the honeycomb network **1Pr**. This study illustrates that minor variations in the size of lanthanide metal ions significantly influence the architecture and application of innovative materials through structural topological isomers.

Received 10th March 2026
Accepted 16th May 2026

DOI: 10.1039/d6ra02049f

rsc.li/rsc-advances

Introduction

In recent decades, the advancement of lanthanide coordination polymers (LnCPs) has emerged as a rapidly expanding area within crystal engineering, structural chemistry, and chemical crystallography.[1] These polymeric organic–inorganic hybrids demonstrate a diverse array of intriguing capabilities such as luminescence sensing, optical characteristics, magnetism, and adsorption, owing to their extraordinary structural diversity.[2] Nonetheless, the rational design and construction of LnCPs with predicted geometries is more challenging than that of d-block metal-based CPs. This is due to the fact that harder Ln^{3+} ions possess larger coordination spheres and exhibit more flexible coordination geometries.[3] Moreover, several parameters such as the metal-to-ligand ratios, solvent, temperature, time, and concentration might affect the self-assembly crystallization of the final structures.[4] Consequently, systematic investigation on these parameters is significant for understanding the structure–property relationship in these materials. In crystal engineering, the rational selection of suitable organic linkers with beneficial characteristics has been demonstrated as a successful strategy for constructing LnCPs with expected structural topologies and desirable attributes.[5] It is widely recognized that Ln^{3+} ions show a high affinity and a strong tendency to coordinate with hard donor atoms. Therefore, multidentate organic ligands featuring oxygen donors, including aliphatic and aromatic polycarboxylic acids, are extensively utilized as foundational components in the synthesis of new LnCPs.[6] Diprotic organic acids including squaric acid (H_2sa), 2,5-dihydroxy-1,4-benzoquinone (H_2dhbq), and chloranilic acid (H_2ca) have been widely used as ligands in

[a]*Thammasat University Research Unit for Multifunctional Crystalline Materials and Applications, Faculty of Science and Technology, Thammasat University, Pathum Thani, 12121, Thailand. E-mail: kc@tu.ac.th*

[b]*Thailand Institute of Nuclear Technology (Public Organization), Nakhon Nayok, 26120, Thailand*

[c]*National Nanotechnology Center (NANOTEC), National Science and Technology Development Agency (NSTDA), Pathum Thani, 12120, Thailand*

[d]*Department of Chemistry, Faculty of Science, Chulalongkorn University, Bangkok, 10330, Thailand*

[e]*Center of Excellence on Petrochemical and Materials Technology, Chulalongkorn University, Bangkok, 10330, Thailand*

the development of functional coordination chemistry involving Ln^{3+} metals.[7] The deprotonation of two hydroxy groups led to a dianion molecule featuring a highly delocalized π-conjugated electron system, which originated from the parent quinone.[8] The stability and reactivity of molecules could possibly be enhanced by these features. LnCPs usually exhibit 3D structures and contain coordinated solvents at the metal centers due to the high coordination numbers of Lns. The removal of solvents creates active open metal sites, thereby enhancing adsorption properties. In the meantime, 2D CPs offer a range of distinctive advantages mainly due to their layered structure, greater flexibility, and excellent processability. With these features such materials can be easily utilized in a wide range of applications including gas storage and separation, catalysis, and electronic devices.[9]

This work presents the synthesis, topological isomers, and CO_2 adsorption properties of 2D LnCPs. Hydrothermal reactions utilizing $LnCl_3$ and H_2ca produced good yields of chloranilate-based LnCPs with excellent repeatability. The compounds are classified into two groups and can be chemically formulated as $[Ln(ca)_{1.5}(H_2O)_3]\cdot xH_2O$ (**1Ln**; Ln = Pr, Nd; **2Ln**; Ln = Sm, Eu, Gd, Tb, Dy, Er, Tm, Yb; $x = 3.5$–5), based on results from single crystal X-ray diffraction, elemental analysis, infrared (IR) spectroscopy, and thermogravimetric (TG) analysis. The relationship between structures-physicochemical–adsorption properties of these two structural isomers was examined and discussed. Additionally, the semi-rigid rod 4,4′-bipyridine (4,4′-bipy) was incorporated into the brick-wall 2D networks under hydrothermal conditions, with the aim of potentially constructing a porous 3D pillared framework. This results in the creation a 4,4′-bipy-intercalated network, as illustrated by the Tm- and Yb-containing compounds formulated as $[Ln(ca)_{1.5}(H_2O)_2]\cdot 2H_2O\cdot 4,4'$-bipy (**3Ln**; Ln = Tm, Yb). A detailed analysis of their supramolecular structures is provided comprehensively.

Experimental

Materials and methods

All commercially available chemicals and solvents were of reagent grade and were used as received without any further purification. Analyses of carbon, hydrogen, and nitrogen were performed using an LECO CHNS 932 elemental analyzer. IR spectra were acquired with a Bruker INVENIO R spectrometer in ATR mode, in the range of 400–4000 cm^{-1}. TG analysis was conducted using a TGA55 TA instrument over a temperature range of 30–800 °C, with a heating rate of 10 °C min^{-1} in a N_2 atmosphere. Powder X-ray diffraction (PXRD) studies were performed utilizing a Rigaku SmartLab2 X-ray diffractometer equipped with graphite monochromatized Cu-Kα radiation (λ = 1.54056 Å) at 30 kV and 10 mA. The simulated XRD patterns were generated from single-crystal X-ray diffraction data and processed using the Mercury software (version 2024.3.1) from the Cambridge Crystallographic Data Centre.[10] The adsorption–desorption isotherms of CO_2 were determined using a Quantachrome Autosorb iQ volumetric analyzer. High-pressure volumetric sorption isotherms for CO_2 were obtained in a pressure range of 0.1–20 bar and at temperature of 318 K using a Quantachrome iSorb HP1 analyzer. All experiments employed CO_2 with a purity of 99.995%.

Synthesis and crystallization

Compounds of the series **1Ln**, $[Ln(ca)_{1.5}(H_2O)_3]\cdot 5H_2O$ (Ln = Pr, Nd) and **2Ln** $[Ln(ca)_{1.5}(H_2O)_3]\cdot 3.5H_2O$ (Ln = Sm, Eu, Gd, Tb, Dy, Er, Tm, Yb) were synthesized under hydrothermal conditions. Typically, a mixture of $LnCl_3\cdot 6H_2O$ (0.1 mmol) and H_2ca (0.1 mmol) in distilled H_2O (4 mL) were placed in a 20 mL vial and stirred at ambient temperature for 10 min. The mixture was sealed tightly, placed in an oven, and then heated to 85 °C for a duration of 12 h. The reaction mixture was allowed to cool, subsequently filtered, washed with water, and dried at ambient temperature before further characterisation.

1Pr. Brown hexagonal crystals with yields of 68% based on the Pr^{3+} source. Anal. calc. for $C_9H_{18}Cl_3O_{15}Pr$: C 17.62, H: 2.96, N 0.00%; found: C 17.34, H 3.12, N 0.00%. IR (ATR, ν/cm^{-1}, s for strong, m medium, w weak): 3401 (m), 1777 (w), 1762 (w), 1613 (m), 1596 (s), 1509 (s), 1384 (s), 1358 (m), 1315 (s), 1299 (w), 1058 (w), 1033 (w), 1000 (w), 845 (m), 800 (m).

1Nd. Brown hexagonal crystals with yields of 72% based on the Nd^{3+} source. Anal. calc. for $C_9H_{18}Cl_3NdO_{15}$: C 17.53, H 2.94, N 0.00%; found: C 17.69, H 2.88, N 0.00%. IR (ATR, ν/cm^{-1}): 3401 (m), 1760 (w), 1613 (m), 1595 (s), 1510 (s), 1381 (s), 1359 (m), 1313 (s), 1294 (w), 1058 (w), 1033 (w), 1001 (w), 846 (m), 798 (m).

2Sm. Brown hexagonal crystals with yields of 79% based on the Sm^{3+} source. Anal. calc. for $C_9H_{13}Cl_3O_{12.5}Sm$: C 18.56, H 2.34, N 0.00%; found: C 18.85, H 2.40, N 0.00%. IR (ATR, ν/cm^{-1}): 3402 (m), 1762 (w), 1613 (m), 1481 (s), 1381 (s), 1258 (w), 1059 (w), 1033 (w), 1004 (m), 846 (s).

2Eu. Brown hexagonal crystals with yields of 75% based on the Eu^{3+} source. Anal. calc. for $C_9H_{13}Cl_3EuO_{12.5}$: C 18.65, H 2.26, N 0.00%; found: C 18.73, H 2.09, N 0.00%. IR (ATR, ν/cm^{-1}): 3401 (m), 1762 (w), 1613 (m), 1471 (s), 1379 (s), 1255 (w), 1063 (w), 1033 (w), 1004 (m), 846 (s).

2Gd. Brown hexagonal-like shaped crystals with yields of 84% based on the Gd^{3+} source. Anal. calc. for $C_9H_{13}Cl_3GdO_{12.5}$: C 18.49, H 2.24, N: 0.00%; found: C 18.55, H 2.37, N: 0.00%. IR (ATR, ν/cm^{-1}): 3041 (m), 1762 (w), 1613 (m), 1469 (s), 1379 (s), 1256 (w), 1060 (w), 1033 (w), 1005 (m), 846 (s).

2Tb. Brown hexagonal-like shaped crystals with yields of 77% based on the Tb^{3+} source. Anal. calc. for $C_9H_{13}Cl_3O_{12.5}Tb$: C C: 18.43, H 2.23, N: 0.00%; found: C 18.51, H 2.37, N: 0.00%. IR (ATR, ν/cm^{-1}): 3401 (m), 1761 (w), 1613 (m), 1503 (w), 1456 (s), 1379 (s), 1257 (w), 1059 (w), 1033 (w), 1005 (m), 847 (s).

2Dy. Brown hexagonal-like shaped crystals with yields of 84% based on the Dy^{3+} source. Anal. calc. for $C_9H_{13}Cl_3DyO_{12.5}$: C 18.21, H, 2.28, N: 0.00%; found: C 18.48, H, 2.15, N: 0.00%. IR (ATR, ν/cm^{-1}): 3400 (m), 1762 (w), 1613 (m), 1502 (w), 1456 (s), 1379 (s), 1300 (w), 1256 (w), 1059 (w), 1033 (w), 1006 (m), 847 (s).

2Er. Brown hexagonal-like shaped crystals with yields of 88% based on the Er^{3+} source. Anal. calc. for $C_9H_{13}Cl_3ErO_{12.5}$: C 18.17, H 2.20, N 0.00%; found: C 18.26, H 2.34, N 0.00%. IR (ATR, ν/cm^{-1}): 3401 (m), 1762 (w), 1613 (m), 1502 (w), 1456 (s), 1379 (s), 1257 (w), 1060 (w), 1033 (w), 1006 (m), 847 (s).

2Tm. Brown hexagonal-like shaped crystals with yields of 82% based on the Tm^{3+} source. Anal. calc. for $C_9H_{13}Cl_3O_{12.5}Tm$: C 18.12, H 2.20, N 0.00%; found: C 18.01, H 2.31, N 0.00%. IR (ATR, ν/cm^{-1}): 3406 (m), 1762 (w), 1613 (m), 1462 (w), 1380 (s), 1257 (w), 1059 (w), 1033 (w), 1006 (m), 847 (s).

2Yb. Brown hexagonal-like shaped crystals with yields of 90% based on the Yb^{3+} source. Anal. calc. for $C_9H_{14}Cl_3O_{13}Yb$: C 18.00, H 2.18, N 0.00%; found: C 18.09, H 2.22, N 0.00%. IR (ATR, ν/cm^{-1}): 3401 (m), 1762 (w), 1613 (m), 1456 (s), 1379 (s), 1249 (w), 1059 (w), 1033 (w), 1007 (m), 847 (s).

Compounds of the series **3Ln**, $[Ln(ca)_{1.5}(H_2O)_2]\cdot 2H_2O\cdot 4,4'$-bipy (Ln = Tm, Yb), were prepared by adding one equivalent of 4,4′-bipy into a crystalline sample of **2Ln**, following the identical synthetic procedures as **1Ln** and **2Ln**.

3Tm. Dark purple block shaped crystals with yields of 62% based on the Tm^{3+} source. Anal. calc. for $C_{19}H_{16}Cl_3N_2O_{10}Tm$: C 32.25, H 2.28, N: 3.96%; found C 32.31, H 2.17, N: 3.86%. IR (ATR, ν/cm^{-1}): 3614 (m) 3531 (m), 1699 (m), 1623 (m), 1600 (m), 1561 (m), 1484 (s), 1432 (s), 1370 (s), 1295 (m), 1095 (m), 1061 (w), 1001 (m), 848 (s), 808 (s), 738 (m), 680 (m).

3Yb. Dark purple block shaped crystals with yields of 51% based on the Yb^{3+} source. Anal. calc. for $C_{19}H_{16}Cl_3N_2O_{10}Yb$: C 32.06, H: 2.27, N: 3.94%; found C 32.11, H 2.29, N 3.95%. IR (ATR, ν/cm^{-1}): 3531 (m), 1670 (m), 1623 (m), 1600 (m), 1560 (m), 1483 (s), 1432 (s), 1369 (s), 1295 (m), 1095 (m), 1059 (w), 1002 (m), 848 (s), 738 (m), 680 (m).

X-ray crystallography

Single crystals of all compounds were carefully mounted on MiTeGen micromounts using paratone oil. X-ray diffraction data were obtained utilizing a Bruker D8 QUEST CMOS PHOTON II at a temperature of 296(2) K. The data were collected using Mo-K_α radiation (λ = 0.71073 Å) through omega and phi scans. The APEX6 software performed strategic calculations to calculate the overall number of runs and images, and SAINT refined unit cell indexing.[11] SAINT was used for data reduction, and SADABS for absorption correction. The integrity of the symmetry was verified using PLATON.[12] The structures were determined using the algorithm implemented in SHELXT[13] *via* intrinsic phasing, followed by refinement through least squares

Table 1 Crystallographic data for all compounds in the series **1Ln–3Ln**

Compound (CCDC)	**1Pr** (2532672)	**1Nd** (2532673)	**2Sm** (2532674)	**2Eu** (2532675)	**2Gd** (2532676)	**2Tb** (2532677)
Formula	$C_9H_{18}Cl_3O_{15}Pr$	$C_9H_{18}Cl_3NdO_{15}$	$C_9H_{13}Cl_3O_{12.5}Sm$	$C_9H_{13}Cl_3EuO_{12.5}$	$C_9H_{13}Cl_3GdO_{12.5}$	$C_9H_{13}Cl_3TbO_{12.5}$
Formula weight	613.49	616.82	582.40	579.50	584.79	586.46
Temperature (K)	296(2)	296(2)	296(2)	296(2)	296(2)	296(2)
Crystal system	Triclinic	Triclinic	Triclinic	Triclinic	Triclinic	Triclinic
Space group	$P\bar{1}$	$P\bar{1}$	$P\bar{1}$	$P\bar{1}$	$P\bar{1}$	$P\bar{1}$
a (Å)	9.9173(8)	9.8881(4)	9.3868(3)	9.3530(3)	9.3410(3)	9.2918(3)
b (Å)	10.0358(9)	10.0028(4)	10.2842(3)	10.2576(3)	10.2493(3)	10.2132(3)
c (Å)	11.1647(10)	11.1361(4)	10.8837(4)	10.8835(4)	10.9033(4)	10.8882(4)
α (°)	88.905(3)	89.059(2)	64.594(1)	64.711(1)	64.837(1)	64.990(1)
β (°)	84.580(3)	84.379(2)	69.763(1)	69.823(1)	69.948(1)	70.009(1)
γ (°)	67.775(3)	67.8480(10)	82.487(1)	82.333(1)	82.218(1)	82.027(1)
V (Å)	1023.88(16)	1015.00(7)	890.28(5)	886.03(5)	887.47(5)	879.95(5)
Z	2	2	2	2	2	2
ρ_{calcd} (g cm^{-3})	1.990	2.018	2.173	2.172	2.202	2.213
λ (Å)	0.71073	0.71073	0.71073	0.71073	0.71073	0.71073
$R[F^2 > 2\sigma(F^2)]$, w$R(F^2)$	0.0294, 0.0720	0.0330, 0.0748	0.0217, 0.0397	0.0306, 0.0531	0.0336, 0.0669	0.0335, 0.0510
GOF on F^2, S	1.06	1.08	1.09	1.08	1.07	1.05
$\Delta\rho_{max}$, $\Delta\rho_{min}$	0.50, −0.77	1.02, −0.78	1.24, −0.58	1.06, −0.94	1.69, −1.28	1.51, −1.45

Compound	**2Dy** (2532678)	**2Er** (2532679)	**2Tm** (2532680)	**2Yb** (2532681)	**3Tm** (2532682)	**3Yb** (2532683)
Formula	$C_9H_{13}Cl_3DyO_{12.5}$	$C_9H_{13}Cl_3ErO_{12.5}$	$C_9H_{13}Cl_3TmO_{12.5}$	$C_9H_{13}Cl_3YbO_{12.5}$	$C_{19}H_{16}Cl_3N_2O_{10}Tm$	$C_{19}H_{16}Cl_3N_2O_{10}Yb$
Formula weight	590.04	594.80	596.47	600.58	707.62	711.73
Temperature (K)	296(2)	296(2)	296(2)	296(2)	296(2)	296(2)
Crystal system	Triclinic	Triclinic	Triclinic	Triclinic	Monoclinic	Monoclinic
Space group	$P\bar{1}$	$P\bar{1}$	$P\bar{1}$	$P\bar{1}$	$P2_1/c$	$P2_1/c$
a (Å)	9.2734(3)	9.2039(5)	9.1844(3)	9.3530(3)	13.003(3)	12.9769(11)
b (Å)	10.2087(3)	10.1659(5)	10.1584(3)	10.2576(3)	13.505(2)	13.5156(12)
c (Å)	10.9033(4)	10.9042(5)	10.8980(4)	10.8835(4)	14.591(3)	14.5543(13)
α (°)	65.088(1)	65.318(2)	65.412(1)	64.711(1)	90	90
β (°)	70.104(1)	70.294(2)	70.356(1)	69.823(1)	107.155(7)	107.308(3)
γ (°)	81.891(1)	81.578(2)	81.469(1)	82.333(1)	90	90
V (Å)	880.29(5)	872.74(8)	870.72(5)	886.03(5)	2448.3(8)	2437.1(4)
Z	2	2	2	2	4	4
ρ_{calcd} (g cm^{-3})	2.226	2.263	2.275	2.251	1.920	1.940
λ (Å)	0.71073	0.71073	0.71073	0.71073	0.71073	0.71073
$R[F^2 > 2\sigma(F^2)]$, w$R(F^2)$	0.0316, 0.0519	0.0230, 0.0444	0.0279, 0.0476	0.0235, 0.0431	0.0218, 0.0473	0.0235, 0.0431
GOF on F^2, S	1.09	1.08	1.12	1.11	1.08	1.11
$\Delta\rho_{max}$, $\Delta\rho_{min}$	1.31, −0.94	1.48, −1.19	2.33, −1.41	1.81, −1.05	0.70, −0.66	0.92, −0.86

on F^2 using SHELXL[14] within the Olex2-1.5 graphical user interface.[15] All non-hydrogen atoms were found in the different Fourier maps and were refined anisotropically in the final refining cycles. The disordered water oxygen atoms were purified to an occupancy of one, and their hydrogen atoms were positioned based on calculations and refined utilizing a riding model. Table 1 shows the crystallographic information for the compounds in the series **1Ln–3Ln**, which have been deposited at the Cambridge Crystallographic Data Centre under CCDC numbers (2532672–2532683).

Results and discussion

Structural description

The single crystal X-ray diffraction study demonstrates that all compounds in series **1Ln** and **2Ln** are isostructural, crystallizing in the triclinic space group $P\bar{1}$, consistent with the previously reported crystal structures by Robson *et al.*[7a] The asymmetric unit comprises one crystallographically distinct Ln^{3+} ion, three half-occupied ca^{2-} anions situated at crystallographic inversion centres, three coordinated water molecules, and five lattice water molecules. As seen in Fig. 1a, the Ln^{3+} ion in both series **1Ln** and **2Ln** shows similar nine-coordinate arrangement, however, an analysis conducted with SHAPE software[16] reveals that the coordination geometry around the core metal center is distinct (Table S1). Accordingly, a capped cube (JCCU-9, C_{4v}) for **1Ln** and a Johnson triangular cupola J3 (JTC-9, C_{3v}) for **2Ln**, Fig. 1b, represent the best described coordination polyhedral of the metal center. The analysis of Ln–O bond lengths in different compounds reveals a decrease in distances corresponding to the decreasing ionic radius of the Ln^{3+} ions (Table S2), from Pr^{3+} to Yb^{3+}, consistent with the lanthanide contraction effect.[17]

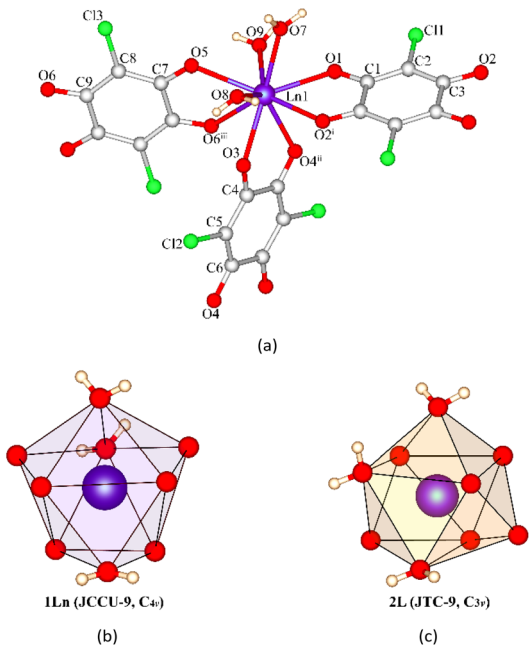

Fig. 1 (a) The coordination environment of the Ln^{3+} ion in the representative compounds of the series. The coordination polyhedron of a central Ln^{3+} ion for (b) **1Ln** and (c) **2Ln**.

The ca^{2-} dianion in a series of compounds behaves as a bidentate bis-chelating ligand, connecting two Ln^{3+} centres *via* a μ_2-κ^2O,O′:κ^2O″,O‴ coordination mode. Consequently, two intriguing geometric motifs of the (6^3) topological networks are established, consisting of alternating three-connected Ln^{3+} nodes and the ca^{2-} ligands acting as linear linkers that form six-membered rings. As shown in Fig. 2(a), the geometric motif of **1Ln** is identified as honeycomb (**hcb**), distinguished by nearly planar hexagonal symmetry with a deviation of approximately 6° from the mean plane, attributed to the incorporation of semi-rigid ca^{2-} ligands. In hexagons, the angles around the three-connected metal nodes are roughly 105°, 115°, and 135°, which deviates from the ideal angle (120°). The dimensions within the hexagon determined through interatomic distance (Ln⋯Ln) are approximately 9.0 × 16.5 Å^2. Along the crystallographic *b* axis, the **hcb** networks of **1Ln** are arranged in a −ABAB− sequence, as depicted in Fig. 2b. This arrangement is likely influenced by the synergistic effects of strong O–H⋯O hydrogen bonding among interlayer water molecules or between water molecules and the oxygen atoms of ca^{2-} ligands (O⋯O = 2.99–3.01 Å), along with Cl⋯Cl and Cl⋯O halogen bonding[18] among the ca^{2-} ligands (Cl⋯Cl/O = 3.21–3.45 Å).

There are lattice water molecules at an interlayer spacing of about 6.1 Å (Ln⋯Ln separation). These water molecules establish hydrogen bonds with each other and with coordinated waters as well as ca^{2-} ligands (O⋯O = 2.83–3.04 Å). In addition, Mercury software[19] was utilized to identify void spaces with a probe radius of 1.2 Å, revealing that **1Ln** possesses a potential void space of 41–45% per unit cell after the complete removal of water molecules, as seen in Fig. 2(c). The significant volume of voids suggests that the material may be suitable for gas adsorption applications.

The change in angles surrounding the metal center from hexagonal **hcb** results in a change of the geometric pattern into a brick-wall rectangular grid motif present in the network of **2Ln**, Fig. 3(a). The angles in hexameric $[Ln_6(ca)_6(H_2O)_{18}]$ units are about 76°, 96°, and 170°, deviating from the ideal angles of 90° and 180° that define a perfect rectangular grid. The dimensions of the grid are approximately 8.1 × 17.6 Å^2. The distances between the Ln atoms along the ca^{2-} bridging ligand vary from 8.6 to 8.9 Å, while the shortest diagonal distance between Ln atoms in the rectangular grid is about 7.5 Å. As shown in Fig. 3(b), the crystal packing of **2Ln** exhibits parallel layers of brick-wall patterns arranged in a −ABAB− pattern similar to that seen in **1Ln**, with a comparable interlayer spacing of around 6.3. Å. The brick-wall interlayers are sustained by O–H⋯O and O–H⋯Cl hydrogen bonding interactions with water molecules or water–ca^{2-} ligands (O⋯O = 2.92–3.08 Å; O⋯Cl = 2.99–3.30 Å) lead to the formation of a 3D supramolecular architecture. No Cl⋯Cl halogen bonding was observed in the crystal packing of **2Ln**, with contacts shorter than the sum of Bondi van der Waals radii (3.5 Å).[20] This lack could account for the presence of topological isomers between **1Ln** and **2Ln**. Additionally, the brick-wall networks of **2Ln** exhibit an estimated guest-accessible volume of 24–28%, as analyzed using Mercury, Fig. 3(c). The void spaces in this series of compounds are approximately 45% smaller than those found in **1Ln**.

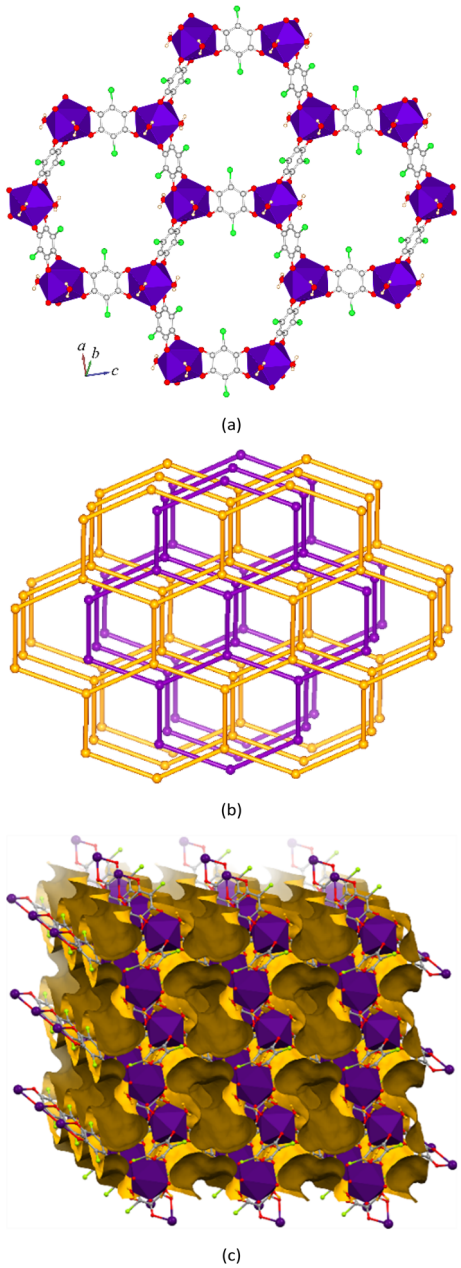

Fig. 2 (a) The 2D **hcb** networks, (b) a schematic representation of the 6^3 topological networks arranged in a –ABAB– stacking sequence, with metal nodes depicted as spheres and ligands as linear rods, and (c) the crystal packing and solvent-accessible surface, analyzed with a probe radius of 1.2 Å using Mercury software for **1Ln**.

Given that aqua ligands in the aforementioned compounds are orientated vertically within the 2D layers, the addition of the rod-like semi-rigid 4,4′-bipy might replace these aqua ligands and potentially lead to the formation of 3D pillared frameworks with porous features. Indeed, appropriate single crystals were obtained from hydrothermal reactions, and single crystal X-ray diffraction analysis clearly demonstrated that the 4,4′-bipy molecules are situated between the 2D layers of 3Ln, forming hydrogen bonds with the aqua ligands. This phenomenon is probably a result of stabilizing interactions formed by strength

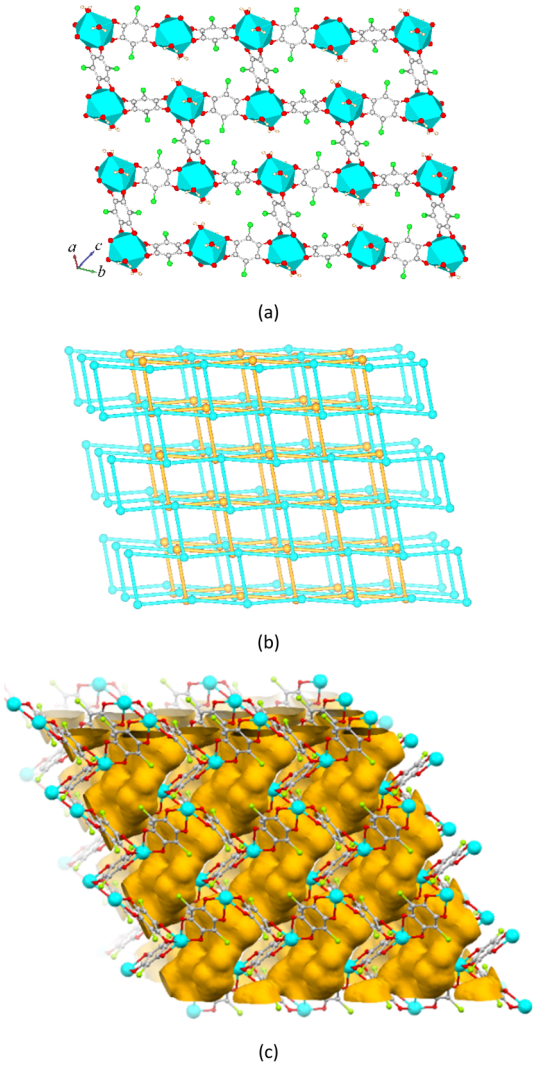

Fig. 3 (a) The 2D brick-wall networks, (b) a schematic illustration of the 6^3 topological networks organized in a –ABAB– stacking sequence, with metal nodes represented as spheres and ligands as linear rods, and (c) the crystal packing and solvent-accessible surface, examined with a probe radius of 1.2 Å utilizing Mercury software for **2Ln**.

and directional O–H···N hydrogen bonding (O···N = 2.99–3.01 Å), which preserves the integrity of the multilayer structure. This interaction may hinder the generation of a fully porous 3D pillared framework, as the existence of 4,4′-bipy molecules may be insufficient to enable the desired structural transformation. Notably, the shortened analogue of compounds like pyrimidine has been employed, nevertheless, crystallization has not been achieved, rendering structural analysis unfeasible.

The layered coordination networks of **3Ln** crystallize in the monoclinic system with the $P2_1/c$ space group. The asymmetric unit of the compounds in series **3Ln** is similar to that of **1Ln** and **2Ln**, consisting of one Ln^{3+} ion and three half-occupied ca^{2-} anions located at the inversion centers, except for the presence of the 4,4′-bipy molecule and the different number of water molecules. As shown in Fig. 4(a), the eight-coordinated Ln^{3+} ion is surrounded by six oxygen atoms from three different ca^{2-}

ligands. According to SHAPE software analysis, the coordination geometry of the core Ln^{3+} ion is a heptagonal pyramid (HPY-8, C_{7v}), depicted in Fig. 4b. The Ln–O bond lengths and the O–Ln–O bond angles of **3Ln** compounds (Table S3) exhibit typical values.[17c] In contrast to the Tm- and Yb-containing compounds within the **2Ln** brick-wall network, the compounds in the **3Ln** series exhibit a distorted **hcb** network. The diameter of the hexagon in the **hcb** network is about 13.7 Å, which corresponds closely with the length of the 4,4′-bipy molecules, allowing it to interact with the terminal aqua ligands through classical hydrogen bonding, Fig. 4(b). The **hcb** networks are arranged along the *b* axis in a –ABAB– manner, creating a 3D supramolecular network through O–H···O hydrogen bonding between lattice water molecules and aqua or ca^{2-} ligands (O···O = 2.88–3.19 Å), C–H···π (C···C_g = 3.02–3.24 Å) interactions among 4,4′-bipy molecules, and Cl···π (Cl···C_g = 3.15–3.27 Å) interactions that involve the ca^{2-} ligands. No aromatic π···π interactions are found between centroids 3.3 to 3.8. Å.[21]

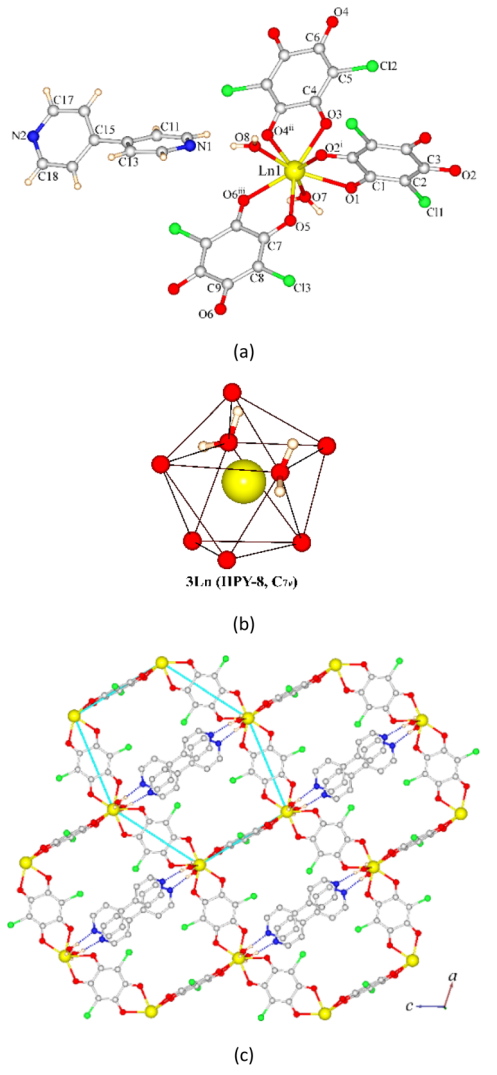

Fig. 4 (a) The coordination environment and (b) the coordination polyhedron of a central Ln^{3+} ion for **3Ln**. (c) The 2D structure of **3Ln**, with the light blue solid lines representing the ca^{2-} ligand that illustrates the hexagon in the **hcb** network.

Physicochemical properties

The powder X-ray diffraction analysis clearly showed distinct patterns among the compounds in the **1Ln** and **2Ln** series, as illustrated in Fig. 5(a). The diffractograms for each series of compounds match closely with the simulated patterns derived from single crystal structural determination, indicating that the compounds possess a well-defined crystalline phase without any significant impurities or defects. The phase purity of the compounds in the **3Ln** is verified by a perfect match between their simulated and experimental diffractogram patterns (Fig. S1). Thus, the synthesis procedures used have shown reliable, allowing for further uses of these compounds. The IR spectra of series **1Ln** and **2Ln** display notable discrepancies in comparison to that of **3Ln** (Fig. S2). However, all compounds in these series display absorption bands at 1625, 1380, 975, and 845 cm^{-1}, signifying the existence of ca^{2-} ligands. The presence of broad bands in the 1500–1450 cm^{-1} range suggests that deprotonated H_2ca increases the aromaticity of ca^{2-} molecules, as evidenced by the C–C stretching vibrations of aromatic rings.[22] The O–H stretching of H_2O molecules is represented by a broad vibration that occurs between 3400 and 3100 cm^{-1}. The characteristic bands of 4,4′-bipyridine molecules in **3Ln** are represented by aromatic C–H (3000–3100 cm^{-1}) and C=C/C=N (1590–1615 cm^{-1}) stretching vibrations.

The TG analysis of compounds in the series **1Ln** and **2Ln** reveals two distinct sets of thermograms, as illustrated in

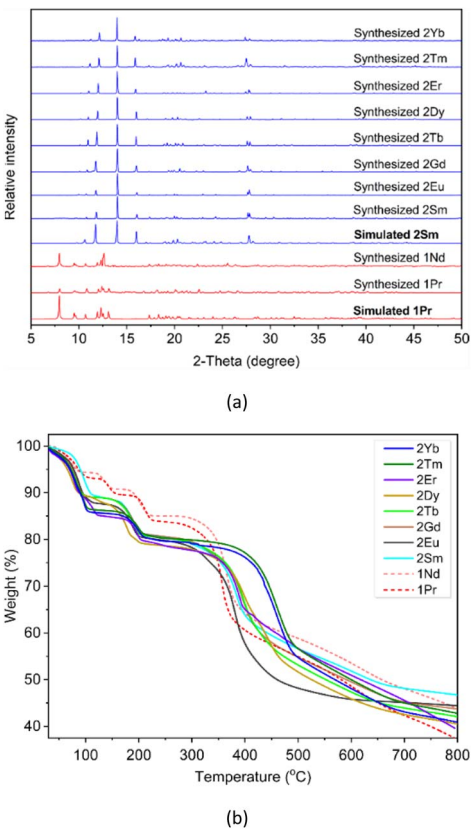

Fig. 5 Comparison of (a) simulated instances with as-synthesized PXRD patterns and (b) TG curves for the compounds in series **1Ln** and **2Ln**.

Fig. 5(b), when subjected to heating in a N_2 atmosphere at a rate of 10 °C min^{-1}. For **1Ln**, the first three stages between room temperature and 225 °C can be attributed to the liberation of five lattice water molecules (found 14.9–15.2%, calc 14.59–14.67%). At about 290 °C, the fourth stage of weight loss took place, probably signifying the loss of coordinated water and ca^{2-} components, accompanied by the collapse of the network. In the case of **2Ln**, the initial two stages of weight loss occurring up to 200 °C can be ascribed to the release of five lattice water molecules (found 19.2–20.2%, calc 17.72–18.40%). The third weight loss observed between 300–400 °C is likely due to the loss of coordinated water and ca^{2-} components, leading to the collapse of the network. The two isomers exhibit distinct decomposition behaviors, influenced by their temperature ranges and mass loss profiles. This highlights how differences in the topological structures of isomeric compounds could impact their thermal stability characteristics.

Carbon dioxide adsorption

Previous studies indicate that 2D layered networks can adsorb CO_2 and exhibit gate-opening behavior under specific pressure and temperature thresholds, thus providing significant insights for their application in carbon capture technology.[23] The **hcb** network **1Pr** and brick-wall network **2Yb** were examined as series examples for their CO_2 adsorption capacities at 1 bar over a temperature range of 273 to 303 K as well as at high pressures up to 20 bar at 298 K. Prior to conducting gas adsorption–desorption tests, the crystalline samples **1Pr** and **2Yb** were activated and dried in a vacuum oven at 100 °C for 12 h, and kept under vacuum overnight. The activated samples were subjected to a 12 h degassing process at 80 °C utilizing the outgas function of the adsorption analyzer. As shown in Fig. 6a,b, neither **1Pr** nor **2Yb** exhibit the gate-opening pressure step for CO_2 sorption at a pressure of up to 1 bar. At temperatures of 273, 298, and 308 K, **1Pr** showed negligible uptakes of 11.42, 5.21, and 3.07 $cm^3\ g^{-1}$, respectively. In contrast, **2Yb** exhibited an increase in uptake compared to **1Pr**, with volumetric values of 30.91, 19.90, and 15.78 $cm^3\ g^{-1}$ at the same temperatures. The desorption branches for **1Pr** exhibited more significant hysteresis than those for **2Yb**. This may result from the differing molecular interactions and structural characteristics of the two isomers.

The CO_2 sorption isotherms for **1Pr** and **2Yb** at 298 K and pressures up to 20 bar, exhibiting a quasi–linear isotherm with the absence of gate opening, as shown in Fig. 6c. **1Pr** displays a maximum CO_2 uptake of 7.05 $cm^3\ g^{-1}$, which is significantly lower than the 34.79 $cm^3\ g^{-1}$ observed for **2Yb.** The higher adsorption capacity of **2Yb** relative to **1Pr** can be attributed to the dimensions and shape the pores, along with variations in the surface areas of their activated samples. These variables contribute to a more extensive and accessible pore network, thereby increasing contact with adsorbates. Notably, the lack of a gate-opening effect in both cases is likely attributable to the structural rigidity of the materials, which limits substantial expansion and conformational changes, hence diminishing their efficacy in situations requiring gate-switching capabilities.

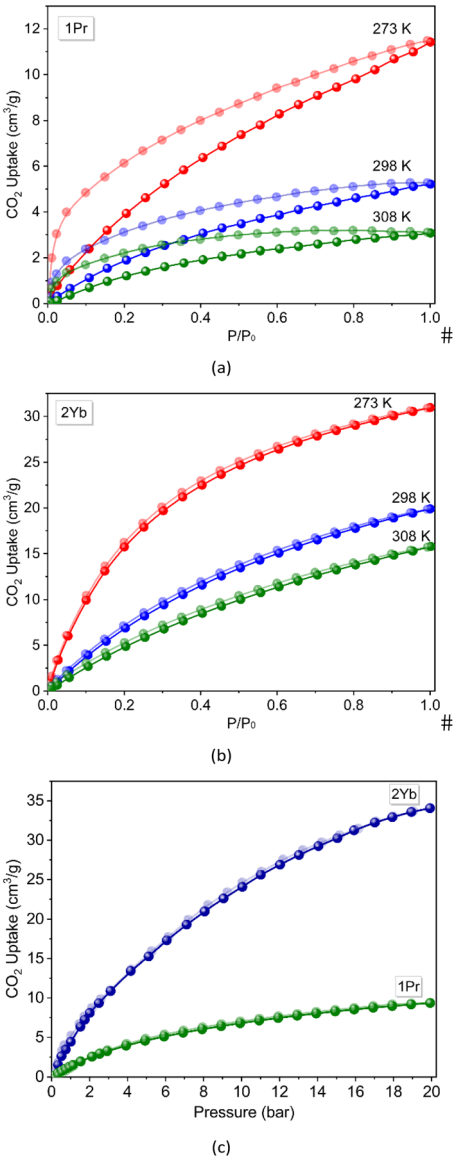

Fig. 6 The adsorption (darker coloured spheres)–desorption (lighter coloured spheres) isotherms for CO_2 at 273, 298, and 308 K in (a) **1Pr** and (b) **2Yb**. (c) High-pressure CO_2 sorption isotherms of **1Pr** and **2Yb** at 298 K.

Additionally, PXRD was performed at ambient temperature to assess the stability of the network or the structural phase transition after thermal activation and gas sorption analyses for instances **1Pr** and **2Yb.** The diffractograms of the synthesized, activated, and after CO_2 sorption experiments exhibit notable differences (Fig. S3), highlighting the distinctive phases and structural features inherent in each sample. A notable change in the main peak positions to higher 2θ values was seen in the diffractograms for **1Pr**, especially in the range of 8.11 to 22.31°. In a similar manner, the diffractogram of the synthesized **2Yb** sample reveals a shift in the main peak positions at 2θ of 10.12, 11.67, and 13.07°, accompanied by the absence of a peak at 15.78°. It was observed that the crystallinity of both **1Pr** and **2Yb** is preserved after CO_2 sorption experiments performed at high

pressures relative to their activated counterparts. Nonetheless, the PXRD profiles for **2Yb** show consistency, while discrepancies are observed in **1Pr**. Moreover, efforts to ascertain the crystal structures of the activated or post-sorption study materials have been futile due to the inadequate diffraction quality of the crystalline samples. This complicates the understanding of the relationships between material structures and CO_2 molecules. Nonetheless, the PXRD findings suggest that **2Yb** retains robust structural integrity under varying pressure conditions, while **1Pr** may undergo more denser structures that could affect its gas sorption efficiency. This difference highlights the importance of materials with different topological isomers in gas adsorption.

Conclusions

In summary, distinct types of lanthanide coordination polymers incorporating the ca^{2-} ligand were successfully synthesized and characterized. The lanthanide contraction influences their two-dimensional structures, leading to the emergence of two unique topological isomers, namely honeycomb **1Ln** and brick-wall **2Ln** arrangements. The incorporation of the semi-rigid rod 4,4′-bipy into brick-wall 2D networks, intended to construct a porous 3D pillared framework, leads to the formation of an intercalation honeycomb network **3Ln** comprising the guest 4,4′-bipy and lattice water molecules. The physicochemical characteristics of the isomers **1Ln** and **2Ln** were distinctly illustrated, emphasizing their unique thermal stability and structural arrangements. The brick-wall network of instance **2Yb** shows better CO_2 adsorption capacities under both ambient and high-pressure conditions compared to **1Pr**, possibly due to its larger pore size and arrangement which leads to a more extensive and accessible pore network. The findings of the present study highlight the complex interplay between structural topological isomers and their properties, demonstrating that even minor differences among lanthanide metals can result in major changes to the structure and functionality of novel materials.

Author contributions

K. K., C. S., P. J., K. C., and S. L.: data collection, formal analysis, visualization, and writing the original draft. B. R.: gas adsorption. M. K.: supervisor. K. C.: conceptualization, formal analysis, writing – review & editing, and funding acquisition. All authors analyzed the results and provided commentary on the manuscript.

Conflicts of interest

There are no conflicts to declare.

Data availability

CCDC 2532672–2532683 **1Ln–3Ln** contain the supplementary crystallographic data for this paper.[24a–l]

The data supporting this article have been included as part of the supplementary information (SI). Supplementary information: lanthanide geometry analysis by SHAPE software, selected bond lengths, IR spectra, and PXRD pattern. See DOI: https://doi.org/10.1039/d6ra02049f.

Acknowledgements

This research received funding from the Faculty of Science and Technology, Thammasat University (SciGR 6/2565), Thammasat Postdoctoral Fellowship (to C. S.), and the National Research Council of Thailand (NRCT): High-Potential Research Team Grant Program (No. 42A690190). K. C. expresses gratitude for the support provided by the Hub of Talent: Sustainable Materials for Circular Economy, NRCT.

References

1 (*a*) K. Bernot, C. Daiguebonne, G. Calvez, Y. Suffren and O. Guillou, *Acc. Chem. Res.*, 2021, **54**, 427–440; (*b*) Y. Hasegawa and Y. Kitagawa, *J. Photochem. Photobiol., A*, 2022, **51**, 100485; (*c*) A. Hauser, L. Münzfeld, C. Uhlmann, S. Lebedkin, S. Schlittenhardt, T.-T. Ruan, M. M. Kappes, M. Ruben and P. W. Roesky, *Chem. Sci.*, 2024, **15**, 1338–1347.

2 (*a*) T. Gorai, W. Schmitt and T. Gunnlaugsson, *Dalton Trans.*, 2021, **50**, 770–784; (*b*) C. Alexander, Z. Guo, P. B. Glover, S. Faulkner and Z. Pikramenou, *Chem. Rev.*, 2025, **125**, 2269–2370; (*c*) M. L. P. Reddy and K. S. Bejoymohandas, *Dalton Trans.*, 2025, **54**, 9441–9452; (*d*) X. Shao, Y. Yang, X. Dong, S. Wang, Y. Liang, Z. Liu, H. Min, Y.-X. Wang and P. Cheng, *Chem. Commun.*, 2025, **61**, 16862–16865; (*e*) Z. W. Jiang, X. Gong, P. Zhang and Y. Wang, *Trends Anal. Chem.*, 2025, **184**, 118133.

3 (*a*) K. Bernot, C. Daiguebonne, G. Calvez, Y. Suffren and O. Guillou, *Acc. Chem. Res.*, 2021, **54**, 427–440; (*b*) S. Li, S. Jansone-Popova and D.-e. Jiang, *Sci. Rep.*, 2024, **14**, 11301; (*c*) J. Zhou, X. Hu, C. Liu, Y. Liu, N. Tian, F. Wu, W. Li, J. Lei and Z. Dai, *Coord. Chem. Rev.*, 2025, **534**, 216574; (*d*) H. Yang, S. Zhao, W. Song, X. Zhao, B. Zhang, R. He and Y. Wang, *Inorg. Chem.*, 2026, **65**, 2980–2996.

4 (*a*) S. Jiajaroen, W. Dungkaew, F. Kielar, M. Sukwattanasinitt, S. Sahasithiwat, H. Zenno, S. Hayami, M. Azam, S. I. Al-Resayesh and K. Chainok, *Dalton Trans.*, 2022, **51**, 7420–7435; (*b*) B. P. Carpenter, A. R. Talosig, B. Rose, G. D. Palma and J. P. Patterson, *Chem. Soc. Rev.*, 2023, **52**, 6918–6937.

5 (*a*) N. Dannenbauer, P. R. Matthes, T. P. Scheller, J. Nitsch, S. H. Zottnick, M. S. Gernert, A. Steffen, C. Lambert and K. Müller-Buschbaum, *Inorg. Chem.*, 2016, **55**, 7396–7406; (*b*) K. Chainok, N. Ponjan, C. Theppitak, P. Khemthong, F. Kielar, W. Dungkaew, Y. Zhou and S. R. Batten, *CrystEngComm*, 2018, **20**, 7446–7457; (*c*) M. Boone, F. Artizzu, J. Goura, D. Mara, R. V. Deun and M. D'hooghe, *Coord. Chem. Rev.*, 2024, **501**, 215525; (*d*) A. K. K. Arachchige, B. Lottes, D. K. Unruh, S. M. Greer, B. W. Stein and K. P. Carter, *Dalton Trans.*, 2026, **55**, 748–760.

6 (*a*) W.-J. Yu, X. Chen, J. Li, B. Li, T.-l. Zhang and J. Tao, *CrystEngComm*, 2013, **15**, 7732–7739; (*b*) W. Lu, Z. Wei, Z.-Y. Gu, T.-F. Liu, J. Park, J. Park, J. Tian, M. Zhang, Q. Zhang, T. Gentle III, M. Bosch and H.-C. Zhou, *Chem. Soc. Rev.*, 2014, **43**, 5561–5593; (*c*) E. R. Engel and

J. L. Scott, *Green Chem.*, 2020, **22**, 3693–3715; (*d*) J. Chen, H. Lu and J. Lin, *Chem. Commun.*, 2025, **61**, 13066–13079; (*e*) K. Patra and H. Pal, *RSC Sustain.*, 2025, **3**, 629–660.

7 (*a*) B. F. Abrahams, J. Coleiro, K. Ha, B. F. Hoskins, S. D. Orcharda and R. Robson, *J. Chem. Soc., Dalton Trans.*, 2002, 1586–1594; (*b*) C. Hua, H. M. Tay, Q. He and T. D. Harris, *Aust. J. Chem.*, 2019, **72**, 778–785; (*c*) S. Konar, A. Mondal and S. Roy, *Chem. - Eur. J.*, 2020, **26**, 8774–8783; (*d*) S. Benmansour, I. Pérez-Herráez, C. Cerezo-Navarrete, G. López-Martínez, C. M. Hernández and C. J. Gómez-García, *Dalton Trans.*, 2018, **47**, 6729–6741; (*e*) S. Benmansour and C. J. Gomez-Garcia, *Magnetochemistry*, 2020, **6**, 71; (*f*) S. Benmansour, C. Pintado-Zaldo, J. Martínez-Ponce, A. Hernández-Paredes, A. Valero-Martínez, M. Gómez-Benmansour and C. J. Gómez-García, *Cryst. Growth Des.*, 2023, **23**, 1269–1280; (*g*) S. Benmansour, C. Pintado-Zaldo, S. H. Casal-Garcia, J. Martinez-Ponce and C. J. Gomez-Garcia, *Chem. - Eur. J.*, 2024, **30**, e2024004.

8 (*a*) J.-F. Petit, A. Gleizes and J.-C. Trombe, *Inorg. Chim. Acta*, 1990, **167**, 51–68; (*b*) B. F. Abrahams, T. A. Hudson, L. J. McCormick and R. Robson, *Cryst. Growth Des.*, 2011, **11**, 2717–2720; (*c*) K. V. Nielson, L. Zhang, Q. Zhang and T. L. Liu, *Inorg. Chem.*, 2019, **58**, 10756–10760; (*d*) K. Kon, K. Uchida, K. Fuku, S. Yamanaka, B. Wu, D. Yamazui, H. Iguchi, H. Kobayashi, Y. Gambe, I. Honma and S. Takaishi, *ACS Appl. Mater. Interfaces*, 2021, **13**, 38188–38193; (*e*) D. Yamazui, K. Uchida, S. Koyama, B. Wu, H. Iguchi, W. Kosaka, H. Miyasaka and S. Takaishi, *ACS Omega*, 2022, **7**, 18259–18266; (*f*) X.-Z. Wang, Y. Chen, X.-M. Cao, R.-Y. Li, W.-Y. Chen, Y. Li and D.-S. Guo, *Angew. Chem., Int. Ed.*, 2025, **137**, e202413115.

9 (*a*) Y. Hijikata, S. Horike, M. Sugimoto, M. Inukai, T. Fukushima and S. Kitagawa, *Inorg. Chem.*, 2013, **52**, 3634–3642; (*b*) S. Hiraide, Y. Sakanaka, H. Kajiro, S. Kawaguchi, M. T. Miyahara and H. Tanaka, *Nat. Commun.*, 2020, **11**, 3867; (*c*) D. Pandey, T. Samarth, V. K. Verma, C. Patel, L. Ponvijayakanthan, N. K. Jaiswal, S. Mukherjee and A. Raghuvanshi, *J. Mater. Chem. A*, 2025, **13**, 11416–11424.

10 C. F. Macrae, I. Sovago, S. J. Cottrell, P. T. A. Galek, P. McCabe, E. Pidcock, M. Platings, G. P. Shields, J. S. Stevens, M. Towler and P. A. Wood, *J. Appl. Crystallogr.*, 2020, **53**, 226–235.

11 Bruker, *APEX6, SAINT, and SADABS*, Bruker AXS Inc., Madison, Wisconsin, USA, 2023.

12 A. L. Spek, *Acta Crystallogr., Sect. C: Struct. Chem.*, 2015, **71**, 9–18.

13 G. M. Sheldrick, *Acta Crystallogr., Sect. A: Found. Crystallogr.*, 2015, **71**, 3–8.

14 G. M. Sheldrick, *Acta Crystallogr., Sect. C: Struct. Chem.*, 2015, **71**, 3–8.

15 O. V. Dolomanov, L. J. Bourhis, R. J. Gildea, J. A. K. Howard and H. Puschmann, *J. Appl. Crystallogr.*, 2009, **42**, 339–341.

16 M. Llunell, D. Casanova, J. Cirera, J. M. Bofill, P. Alemany, S. Alvarez, M. Pinsky and D. Avnir, *SHAPE, version 2.1*, Universitat de Barcelona and Hebrew University of Jerusalem, 2013.

17 (*a*) S. Sairenji, S. Akine and T. Nabeshima, *Dalton Trans.*, 2016, **45**, 14902–14906; (*b*) J. A. Peters, K. Djanashvili, C. F. G. C. Geraldes and C. Platas-Iglesias, *Coord. Chem. Rev.*, 2020, **406**, 213146; (*c*) S. C. Bart, *Inorg. Chem.*, 2023, **62**, 3713–3714.

18 (*a*) G. Cavallo, P. Metrangolo, R. Milani, T. Pilati, A. Priimagi, G. Resnati and G. Terraneo, *Chem. Rev.*, 2016, **116**, 2478–2601; (*b*) L. Brammer, A. Peuronena and T. M. Rosevearea, *Acta Crystallogr., Sect. C: Struct. Chem.*, 2023, **79**, 204–216; (*c*) S. An and P. Xing, *Chem. Soc. Rev.*, 2026, **55**, 1460–1493.

19 C. F. Macrae, I. Sovago, S. J. Cottrell, P. T. A. Galek, P. McCabe, E. Pidcock, M. Platings, G. P. Shields, J. S. Stevens, M. Towler and P. A. Wood, *J. Appl. Crystallogr.*, 2020, **53**, 226–235.

20 A. Bondi, *J. Phys. Chem.*, 1964, **68**, 441–451.

21 C. Janiak, *J. Chem. Soc., Dalton Trans.*, 2000, 3885–3896.

22 (*a*) R. Ishikawa, S. Michiwaki, T. Noda, K. Katoh, M. Yamashita, K. Matsubara and S. Kawata, *Inorganics*, 2017, **6**, 7; (*b*) P. Zhang, M. Perfetti, M. Kern, P. P. Hallmen, L. Ungur, S. Lenz, M. R. Ringenberg, W. Frey, H. Stoll, G. Rauhut and J. v. Slageren, *Chem. Sci.*, 2018, **9**, 1221–1230; (*c*) R. Ishikawa, S. Michiwaki, T. Noda, K. Katoh, M. Yamashita and S. Kawata, *Magnetochem*, 2019, **5**, 30.

23 (*a*) D. Li and K. Kaneko, *Chem. Phys. Lett.*, 2001, **335**, 50–56; (*b*) Y. Ying, Z. Zhang, S. B. Peh, A. Karmakar, Y. Cheng, J. Zhang, L. Xi, C. Boothroyd, Y. M. Lam, C. Zhong and D. Zhao, *Angew. Chem., Int. Ed.*, 2021, **60**, 11318–11325; (*c*) S. R. Acharya, A. Elias, K. Tan, S. Jensen, R.-B. Lin, B. Chen, M. D. Gross and T. Thonhauser, *Inorg. Chem.*, 2022, **61**, 5025–5032; (*d*) S.-Q. Wang, V. Bon, S. Darwish, S.-M. Wang, Q.-Y. Yang, Z. Xu, S. Kaskel and M. J. Zaworotko, *ACS Mater. Lett.*, 2024, **6**, 666–673; (*e*) M.-Y. Gao, L. Liu, C. Deng, V. Bon, B.-Q. Song, S. Yang, M. Schröder, S. Kaskel and M. J. Zaworotko, *Angew. Chem., Int. Ed.*, 2024, **63**, e202404084.

24 (*a*) CCDC 2532672: Experimental Crystal Structure Determination, 2026, DOI: 10.5517/ccdc.csd.cc2r0g3c; (*b*) CCDC 2532673: Experimental Crystal Structure Determination, 2026, DOI: 10.5517/ccdc.csd.cc2r0g4d; (*c*) CCDC 2532674: Experimental Crystal Structure Determination, 2026, DOI: 10.5517/ccdc.csd.cc2r0g5f; (*d*) CCDC 2532675: Experimental Crystal Structure Determination, 2026, DOI: 10.5517/ccdc.csd.cc2r0g6g; (*e*) CCDC 2532676: Experimental Crystal Structure Determination, 2026, DOI: 10.5517/ccdc.csd.cc2r0g7h; (*f*) CCDC 2532677: Experimental Crystal Structure Determination, 2026, DOI: 10.5517/ccdc.csd.cc2r0g8j; (*g*) CCDC 2532678: Experimental Crystal Structure Determination, 2026, DOI: 10.5517/ccdc.csd.cc2r0g9k; (*h*) CCDC 2532679: Experimental Crystal Structure Determination, 2026, DOI: 10.5517/ccdc.csd.cc2r0gbl; (*i*) CCDC 2532680: Experimental Crystal Structure Determination, 2026, DOI: 10.5517/ccdc.csd.cc2r0gcm; (*j*) CCDC 2532681: Experimental Crystal Structure Determination, 2026, DOI: 10.5517/ccdc.csd.cc2r0gdn; (*k*) CCDC 2532682: Experimental Crystal Structure Determination, 2026, DOI: 10.5517/ccdc.csd.cc2r0gfp; (*l*) CCDC 2532683: Experimental Crystal Structure Determination, 2026, DOI: 10.5517/ccdc.csd.cc2r0ggq.